XIV International Conference on Computational Plasticity. Fundamentals and Applications
COMPLAS XIV
E. Oñate, D.R.J. Owen, D. Peric & M. Chiumenti (Eds)

ON THE ROLE OF PARTICLES AND RADIAL BASIS FUNCTIONS IN A FINITE ELEMENT LEVEL SET METHOD FOR BUBBLE DYNAMICS

JUAN LUIS PRIETO[*] [†]

[†] Departamento de Ingeniería Energética
Escuela Técnica Superior de Ingenieros Industriales
Universidad Politécnica de Madrid
c/ José Gutiérrez Abascal, 2, 28006 Madrid, Spain
e-mail: juanluis.prieto@upm.es
ORCID® iD: orcid.org/0000-0001-5085-0482

Key words: Finite Element Method, Level Set, Particles, Radial Basis Functions, Bubbles, Non-Newtonian Flows.

Abstract. The aim of this presentation is to highlight the role that Particle-based simulations and Radial Basis Functions (RBFs) have played in the development of a computationally efficient, level-set, Finite Element method for the simulation of Newtonian and non-Newtonian interface flows. First, we introduce the mathematical formulation and the interface-capturing technique used in the simulation of multiphase flows, underscoring the influence of marker particles on the enhanced definition of the interface. Then, we explore the effect of adding polymer particles to the domain to perform Brownian Dynamics Simulations of polymer flows. Finally, we leverage RBFs to reconstruct, in an almost free-independent way the polymer stress tensor retrieved from the polymer particles.

Numerical simulations of pure advection flows and bubble dynamics simulations of complex flows on two-dimensional configurations emphasize the improvements offered by this hybrid, Finite Element/RBF/Particle-based method.

1 INTRODUCTION

From its inception, the contribution of meshfree methods to the solution of complex scientific and engineering problems has proven remarkable; at this point in its history, particle and meshless methods offer a viable alternative to more traditional methods [1, 2, 3, 4, 5]. The purpose of this work is to highlight some recent advances made in the field of Multiphase Flows and non-Newtonian Fluid

Dynamics by combining particle methods and Radial Basis Functions with the Finite Element Method in a semi-Lagrangian approach.

2 MATHEMATICAL FORMULATION

Since we aim with this work to illustrate the role of particles in multiphase flows, and more precisely, in bubble dynamics simulations, we succinctly describe here the numerical tools used, referring the reader elsewhere for additional details.

2.1 Marker particles for free-surface representation

As an improvement over the level set method, marker particles can be added to better represent the interface between the two fluids. The idea is to advect the massless particles and provide each of them with a variable radius $r_{\min} \leq r_p \leq r_{\max}$ so that the particle surface, whenever possible, remains in contact with the free-surface; otherwise, the particle will have a minimum or maximum radius. Then, we carry out a three-stage procedure based on error identification, error quantification and error correction, with local level set functions ϕ_p defined at each of the massless particles according to:

$$\phi_p(\mathbf{x}_i) = s_p^n \left(\left| \mathbf{x}_i - \mathbf{x}_p^n \right| - r_p^n \right),$$

with $s_p^n \equiv sign\left\{\phi_h^n(\mathbf{x}_p^n)\right\}$. These particles help in correcting the global level set function ϕ whose zero isocontour represents the interface. For details, see [6].

2.2 Polymer particles in Brownian Dynamics simulations

As an alternative to the constitutive modeling of non-Newtonian fluids, the micro-macro (stochastic) approach uses polymer particles that carry the internal degrees of freedom of the viscoelastic fluid; these particles are advected by the flow, contributing to the incompressible, Navier-Stokes equations through the extra-stress tensor computed by taking moments of the configurations. In this work, we use the Hookean and FENE ('Finitely Extensible, Nonlinear Elastic') kinetic models, each of them represented by two dumbbells connected by a spring of force $\mathbf{F}$, so that the stochastic differential equation ruling the configurations $\mathbf{Q}$ of the dumbbells are integrated by a (weak) second-order algorithm, as in [7, 8]. Further, the cubic equation for the FENE model is efficiently solved with the method proposed in [9]. Variance-reduction techniques are applied using N_{ens} ensembles each of them containing N_d dumbbells, as described in [6].

2.3 CSRBFs for polymer stress tensor reconstruction

Compactly-Supported Radial Basis Functions offer a way of handling, in an efficient and mesh-independent manner, the problem of image reconstruction

from a set of points [10]. In our context, their usefulness directly relates to the reconstruction of the polymer stress tensor: as data set we have the values of each of the components of the polymer stress tensor τ_{pij}^{i} at a certain ensemble i, along with the position of the ensembles themselves $\{\mathbf{x}_i\}$. We choose to use the CSRBFs of minimal degree obtained by Wendland [11], solving the linear systems resulting after imposing the orthogonality conditions using the techniques described in [12].

3 ILLUSTRATIVE EXAMPLES

In this section, we highlight the usefulness of particles and RBFs for improving interface shape, modeling non-Newtonian fluids, and reconstructing the polymer, extra-stress tensor, by a series of numerical tests.

3.1 Star-shaped droplet in vortex flow

We consider the pure advection test recently proposed in [13] to check the ability of the method to deal not only with stretching filaments and quite possibly with topological changes, but also with a multi-layered structure that must be recovered at the end of the periodic simulation. A star-shaped droplet is placed at the center of a square $[0,1]\times[0,1]$ domain, with the interface given in polar coordinates by $r(\theta) = a + b\cos(m\theta)$, with $a = 0.3, b = 0.1$ and $m = 5$. The imposed, periodic ($T_p = 4$) vortex flow is defined by the stream function $\psi = \frac{1}{\pi}\sin^2(\pi x)\sin^2(\pi y)\cos(\pi t/T_p)$, so that the velocity field is obtained as

$$\begin{cases} u = -\sin^2(\pi x)\sin(2\pi y)\cos(\pi t/T_p)\,, \\ v = \sin^2(\pi y)\sin(2\pi x)\cos(\pi t/T_p)\,. \end{cases} \tag{1}$$

Next, we use our SLEIPNNIR method [6] to retrieve the interface at the final instant of the simulation, for a variable number of marker particles scattered in the domain $N_p = \{0, 10^4, 5\times10^4, 10^5\}$; a second-order, eikonal-based reinitialization procedure is used every other time step to ensure that no numerical instabilities propagate away from the interface; the fixed time step size is $\Delta t = 0.01$. A uniform, unstructured mesh refinement was carried out to ascertain the influence of the mesh size h, with h successively halving from $h = 8\times10^{-2}$ down to $h = 5\times10^{-3}$. The shapes of the droplet are pictured in Fig.1: we observe how the addition of marker particles notably improves shape preservation, strikingly so for the coarsest mesh ($h = 8\times10^{-2}$) in which the addition of even a small amount of marker particles ($N_p = 10^4$) enhances the final shape from a rather amorphous interface when no marker particles are used, to a quite precise final shape.

Table 1 conveniently collects the mesh size h, number of elements NE, number of mesh nodes NC, and number of particles N_p used in each simulation, along with the errors measured in the L^2 and L^∞-norms, percentage of mass loss at the end

Figure 1: Shape of a star-shaped droplet in a square $[0,1] \times [0,1]$ domain under a periodic ($T_p = 4$) vortex flow, under uniform mesh refinement. Panels from left to right, and from top to bottom: $h = \left\{8 \times 10^{-2}, 4 \times 10^{-2}, 10^{-2}, 5 \times 10^{-3}\right\}$. For each panel, a variable number of marker particles is used: $N_p = 0$ (green), $N_p = 10^4$ (orange), $N_p = 5 \times 10^4$ (blue) and $N_p = 10^5$ (purple); the initial solution is represented in black.

of the simulation and maximum memory demanded during the simulation. For a fixed mesh size, increasing the number of particles results in a behavior resembling the law of diminishing returns: the benefits of the addition of marker particles are remarkable, while increasing the number offers increasingly small improvements. Nevertheless, the computational cost of the marker particles in terms of memory spent during the simulation, is modest in the coarser meshes and negligible in the finer meshes.

In Fig.2 we plot the evolution of the e_{L^2} error for the three finer meshes and an increasing number of marker particles. As we can observe, the maximum value is reached at the moment of the largest deformation of the flow, decreasing again when particles are added, and slowly increasing in time if no marker particles are used. Again, the same trend of diminishing returns is observed throughout the simulations.

Table 1: Average size h of the unstructured, uniform mesh; number of marker particles N_p; number of elements NE; number of mesh-points NP; error in the Euclidean norm e_{L^2}; error in the infinity norm e_{L^∞}; mass loss percentage; and maximum memory used during the simulation of a periodic ($T_p = 4$) star-shaped droplet under a vortex flow. Values collected at the end of the simulation ($t = 4$).

h	N_p	NE	NC	Error e_{L^2}	Error e_{L^∞}	$A_{\text{loss}}(\%)$	Mem (MB)
$8E{-}2$	0	360	773	$3.1647E{-}1$	$1.1128E{-}1$	$3.81E{-}2$	39.86
$8E{-}2$	10000	362	777	$5.4471E{-}2$	$3.2967E{-}3$	$1.30E{-}2$	40.38
$8E{-}2$	50000	362	777	$6.3726E{-}2$	$4.5122E{-}3$	$6.32E{-}2$	46.87
$8E{-}2$	100000	360	773	$6.9271E{-}2$	$5.3317E{-}3$	$4.02E{-}2$	55.98
$4E{-}2$	0	1484	3069	$2.9478E{-}1$	$9.6547E{-}2$	$2.53E{-}1$	63.44
$4E{-}2$	10000	1484	3069	$3.1659E{-}2$	$1.1137E{-}3$	$3.77E{-}3$	63.39
$4E{-}2$	50000	1484	3069	$2.9832E{-}2$	$9.8883E{-}4$	$9.81E{-}3$	67.47
$4E{-}2$	100000	1484	3069	$2.4658E{-}2$	$6.7557E{-}4$	$8.59E{-}3$	77.23
$2E{-}2$	0	5846	11893	$2.8022E{-}1$	$8.7248E{-}2$	$2.51E{-}3$	142.08
$2E{-}2$	10000	5846	11893	$4.4221E{-}2$	$2.1728E{-}3$	$6.76E{-}2$	142.06
$2E{-}2$	50000	5846	11893	$1.2143E{-}2$	$1.6383E{-}4$	$4.42E{-}4$	142.10
$2E{-}2$	100000	5846	11893	$1.1652E{-}2$	$1.5085E{-}4$	$6.64E{-}4$	142.17
$1E{-}2$	0	23384	47169	$2.1471E{-}1$	$5.1223E{-}2$	$3.61E{-}2$	514.41
$1E{-}2$	10000	23384	47169	$2.0051E{-}2$	$4.4672E{-}4$	$1.88E{-}4$	514.31
$1E{-}2$	50000	23384	47169	$1.1636E{-}2$	$1.5043E{-}4$	$2.27E{-}4$	514.38
$1E{-}2$	100000	23384	47169	$1.0572E{-}2$	$1.2418E{-}4$	$7.75E{-}5$	514.41
$5E{-}3$	0	94330	189461	$9.1740E{-}2$	$9.3514E{-}3$	$3.57E{-}3$	2,029.47
$5E{-}3$	10000	94330	189461	$1.9352E{-}2$	$4.1612E{-}4$	$2.16E{-}4$	2,029.37
$5E{-}3$	50000	94330	189461	$1.0243E{-}2$	$1.1657E{-}4$	$5.29E{-}5$	2,029.48
$5E{-}3$	100000	94330	189461	$8.3215E{-}3$	$7.6941E{-}5$	$5.62E{-}5$	2,029.46

3.2 Viscoelastic droplet in shear flow

We now proceed with a problem in which the viscoelastic effects are present, namely, the behavior of a viscoelastic droplet in a Newtonian, viscous fluid. This situation has been thoroughly investigated (see e.g. [14, 15, 16]) in studies strongly suggesting that droplet viscoelasticity prevents deformation to a certain degree The schematics are showed in Fig.3, in which a droplet of radius a is placed at the center of a domain $[2L \times 2H]$, with $H = 4a$ and $L = 8a$. The no-slip boundary condition is imposed at the bottom and top lids of the domain, which move at a velocity V in opposite directions, giving rise to a shear rate $\dot{\gamma} = V/H$, here taken as $\dot{\gamma} = 1$. For details on the numerical model, refer to the uncorrelated computations found in [6] and [17].

The viscoelastic drop is modeled by Hookean dumbbells (equivalent to the Oldroyd-B constitutive equation), and is immersed in a Newtonian, ambient fluid. The flow is suddenly started at $t = 0$ with shear rate $\dot{\gamma} = 1$, using a mesh with 80×40 elements and $N_p = 10^7$ uncorrelated, polymer particles (dumbbells) uniformly placed inside the droplet; the flow is continued until dimensionless time

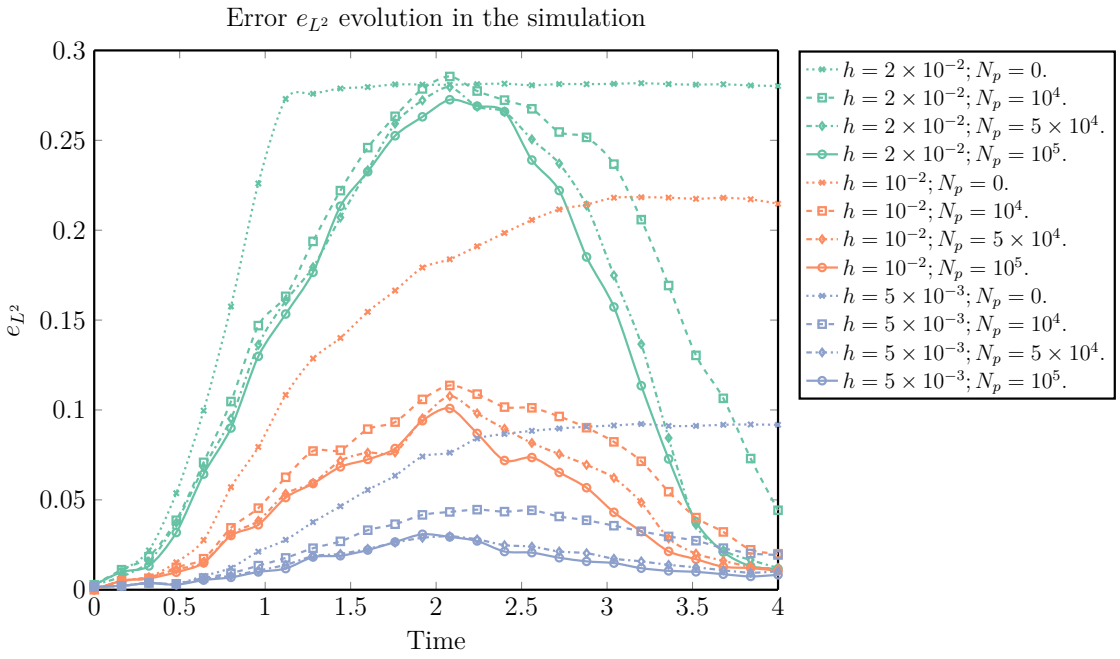

Figure 2: Evolution of the e_{L^2} error during the simulation of a star-shaped droplet in a square $[0,1] \times [0,1]$ domain under a periodic ($T_p = 4$) vortex flow, under uniform mesh refinement $h = \{2 \times 10^{-2}, 10^{-2}, 5 \times 10^{-3}\}$ and variable number of marker particles $N_p = \{0, 10^4, 5 \times 10^4, 10^5\}$.

$t^* = t\dot{\gamma} = 10$, with a small time step to accurately solve the internal configurations of the dumbbells ($dt = 1/200$), taking $N_t = 2000$ time steps to finish each simulation; the number of marker particles to improve the definition of the interface is $N_{mp} = 2.5 \cdot 10^5$. The effects of the Reynolds prove to be of utmost importance, in the sense that, if the method is not able to deal with extremely low Re (creeping flows), the inertial effects become relevant when small time steps are used, thus affecting the history of the flow and, consequently, that of the dumbbells: it is for this reason that $Re = 10^{-5}$ is chosen. The rest of the dimensionless parameters are those found in [14] (also referenced henceforth as "Yue et al. PoF05"): $Fr \to \infty$, $We = 10^{-6}$ so that the Capillary number $Ca = 0.1$; our concentration parameter c, according to the characteristic scales chosen in that article, corresponds to $c = 1 - \beta$, with $\beta = 0.5$ the retardation parameter of the Oldroyd-B fluid; the Deborah numbers studied are $De = \{0.25; 0.5; 1; 2\}$; and the density and viscosity ratios between the droplet and the outer ambient fluid (matrix) are $\rho_2/\rho_1 = \mu_2/\mu_1 = 1$.

We perform a set of simulations to obtain the evolution of the droplet deformation, and compare the results with those by Yue et al. in their Fig.1; the results are collected in Fig. 4. Despite the rather coarse mesh used, the not-so high number of dumbbells, and the totally different approach taken by the two techniques compared (their diffuse-interface method along with a phase-field approach ruled

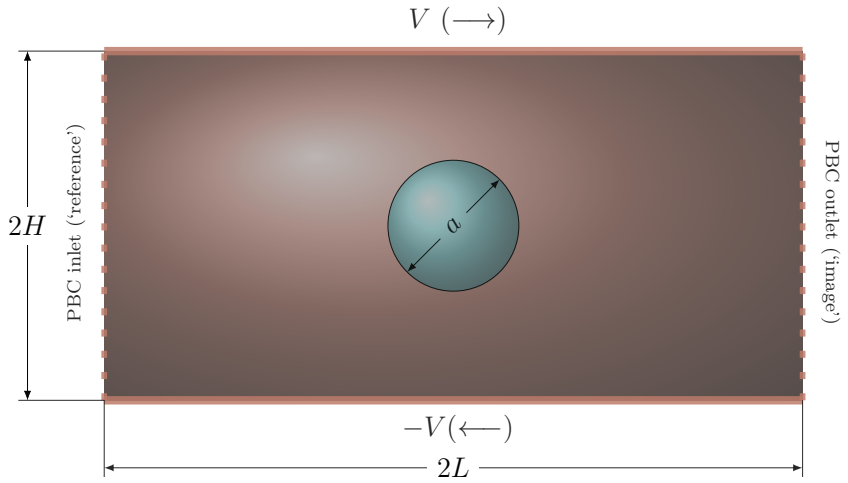

Figure 3: Viscoelastic droplet in Newtonian matrix under a shear flow. Sketch.

by Cahn-Hilliard dynamics to study the Newtonian/non-Newtonian problem in a unified way; and our micro-macro, semi-Lagrangian, Particle Level-Set Finite Element method) the results are in remarkably good agreement, especially the steady state values of the deformation parameter D, defined as $D = (L - B) / (L + B)$, with L and B being the longest and shortest lengths from the center of the droplet to the interface (corresponding also to the major and minor axes of the ellipse), respectively. The transient behavior shows a noteworthy resemblance as well, with the overshoot appearing for sufficiently high De values, and the evolution of $De = 2$ being for $t \lessapprox 4$ being higher than those for $De = 1$. In any case, we notice the effect of the droplet viscoelasticity as a means to reduce the deformation of the interface; plots of the actual shape of the interface (not included here) show this same trend. Finally, we would like to point out that more refined meshes would be needed to prevent some of the oscillation from appearing in the Figure; apart from the stochastic noise (we are using here totally uncorrelated dumbbells), the modification of the interface by the correction stage of the marker particles and the mass conservation step add somewhat to this oscillatory behavior in D, which is explicitly computed from the discrete interface; additional results with a better mesh indeed confirm this fact.

3.3 Reconstruction of polymer stress tensor

Finally, to show the ability of the CSRBFs to reconstruct the extra-stress tensor in non-Newtonian fluids, we perform some numerical tests in a two-dimensional configuration using SLEIPNNIR [6] where a Newtonian bubble rises in a non-Newtonian ambient fluid. A very fine, uniform mesh with grid size $h = 1/320$ is used, with $N_{ens} = 3 \times 10^4$ ensembles being scattered in the viscoelastic fluid,

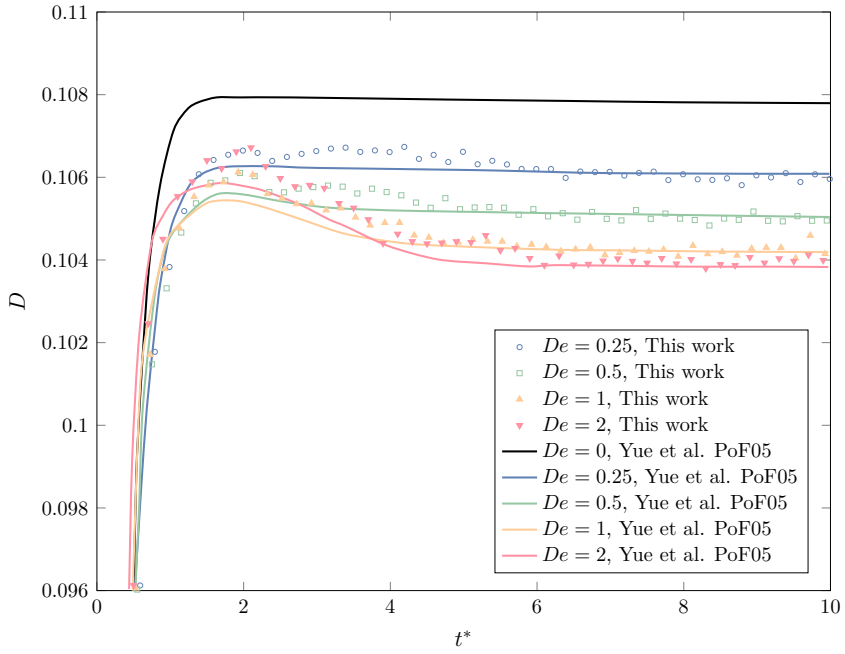

Figure 4: Evolution of the deformation parameter D for a viscoelastic droplet in a Newtonian matrix under a shear flow, for increasing values of the Deborah number De. Comparison with Fig. 1 of [14].

each of them carrying $N_d = 25 \times 10^3$ dumbbells for variance-reduction effects. The dimensionless numbers defining the problem are: Reynolds $Re = 35$, Weber $We = 10$, concentration parameter $c = 5$, Deborah number $De = 3$, density and viscosity ratios $\rho_1/\rho_2 = 10 = \mu_1/\mu_2$; the kinetic FENE ($b = 50$) model is used, with the efficient solution to the resulting cubic equation proposed in [9], and the simulation is continued until dimensionless time $t = 3$ is reached. Four different Compactly-Supported Radial Basis Functions proposed by Wendland are used, with different degree of smoothness represented by the number of continuous derivatives, $\varphi_{sk} \in \mathcal{C}^{2k}(\mathbb{R})$ with convergence rate $h^{s/2+k+1/2}$, and a support size $\chi = 65$. We observe that increased smoothness is beneficial to the reconstruction of well-defined surfaces, with a sufficiently high number of ensembles; see Fig. 5 for the final shapes of the bubbles, in which a nice convergence is noticed for $\varphi_{31}, \varphi_{32}$ and φ_{33}. Additionally, Fig. 6 plots the reconstruction of the shear component of the polymer stress tensor at the end of the simulations; the previous comments may be applied here as well. For additional details about the effect of ensembles and dumbbells per ensemble, see [12].

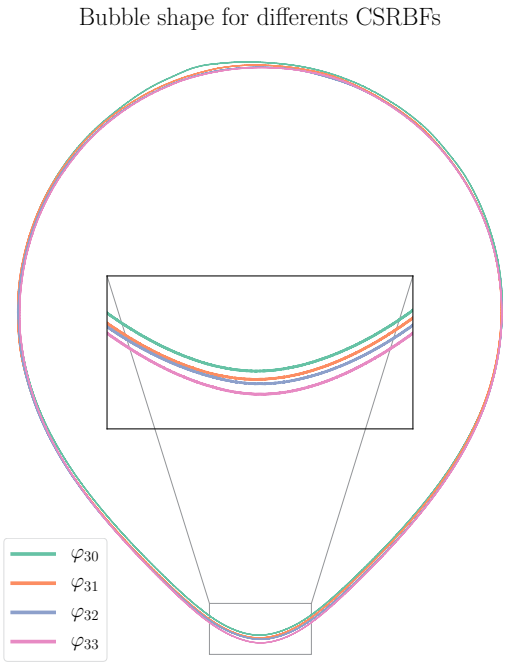

Figure 5: Final shape of bubble using differents CSRBFs: $\varphi_{30}, \varphi_{31}, \varphi_{32}, \varphi_{33}$.

4 CONCLUSIONS

The purpose of this work has been to underscore the role of particles in the context of numerical methods for multiphase flow problems, showing their relevance in a three-fold way:

- Improvement of mass conservation and enhancement of shape preservation, by means of *marker particles*.
- Modeling of non-Newtonian fluids in complex, multiphase flows, using *polymer particles* along with Brownian Dynamics simulations.
- Reconstruction the polymer, extra-stress tensor, leveraging smooth Compactly-Supported Radial Basis Functions.

All these effects have been addressed in a series of numerical simulations that prove the potential of such an approach. Future work involves Adaptive Mesh Refinement techniques, with preliminary results recently communicated in [18].

5 ACKNOWLEDGMENTS

Financial support from grant MTM2015-67030-P from Ministerio de Economía y Competitividad is acknowledged.

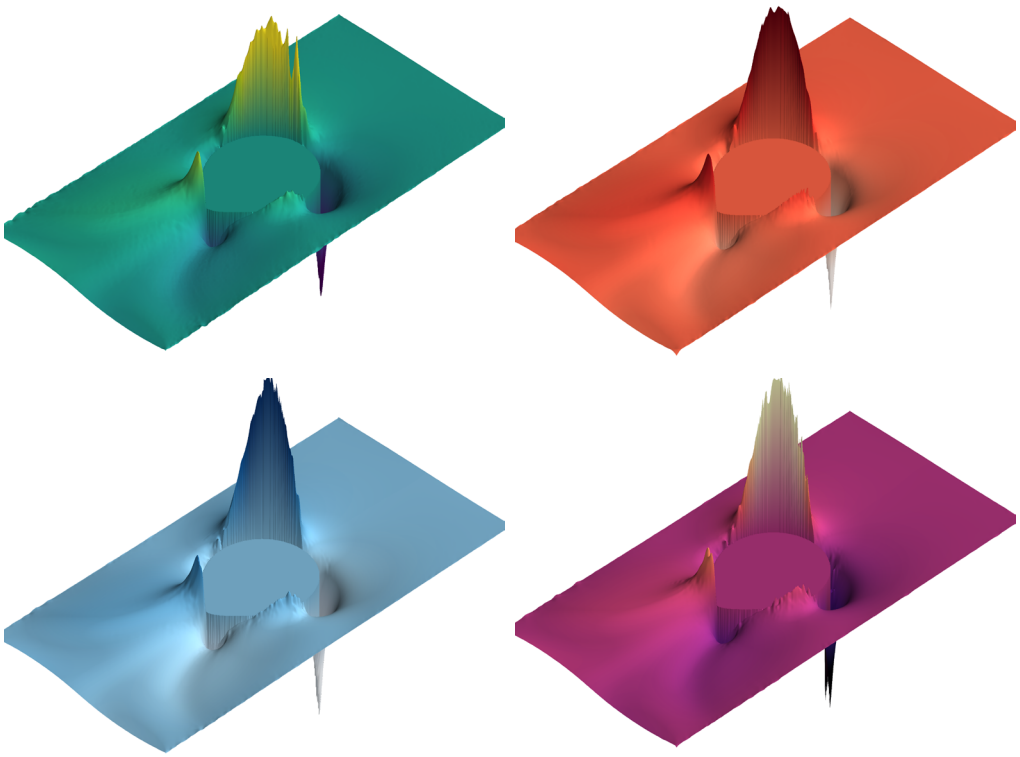

Figure 6: Reconstruction of the shear component τ_{p12} of the polymer stress tensor at the end of a bubble dynamics simulation, for different Wendland's CSRBFs. Panels from left to right, and from top to bottom: $\varphi_{30}, \varphi_{31}, \varphi_{32}, \varphi_{33}$.

REFERENCES

[1] Ferreira, A.J.M. , Roque, C.M.C. and Jorge, R.M.N. Free vibration analysis of symmetric laminated composite plates by FSDT and radial basis functions. *Comput. Methods Appl. Mech. Engrg.* (2005) **194**(39-41):4265–4278.

[2] Nguyen, V.P., Rabczuk, T., Bordas, S. and Duflot, M. Meshless methods: A review and computer implementation aspects. *Mathematics and Computers in Simulation* (2008) **79**(3):763–813.

[3] Liu, G. R. *Meshfree methods: moving beyond the finite element method*. CRC press, (2009), ISBN: 9781420082098.

[4] Belinha, J., Dinis, L.M.J.S. and Jorge, R.M.N., The natural radial element method. *Int. J. Numer. Meth. Engrg.* (2013) **93**(12):1286–1313.

[5] Griebel, M. and Schweitzer, M.A. (Eds.). *Meshfree Methods for Partial Differential Equations VIII*. Springer, (2017), ISBN: 978-3-319-51954-8.

[6] Prieto, J.L., SLEIPNNIR: A multiscale, particle level set method for Newtonian and non-Newtonian interface flows. *Comput. Methods Appl. Mech. Engrg.* (2016) **307**:164–192.

[7] Öttinger, H.C. *Stochastic Processes in Polymeric Fluids*. Springer, (1996), ISBN: 978-3-642-58290-5.

[8] Prieto, J.L., Stochastic particle level set simulations of buoyancy-driven droplets in non-Newtonian fluids. *J. Non-Newtonian Fluid Mech.* (2015) **226**:16–31.

[9] Prieto, J.L., Multi-scale Simulation of Newtonian and Non-Newtonian Multiphase Flows. In: Ibrahimbegovic, A. (Ed.). *Computational Methods for Solids and Fluids: Multiscale Analysis, Probability Aspects and Model Reduction*. Springer, Computational Methods in Applied Sciences series, Vol. 41 (2016):379–398. ISBN: 978-3-319-27996-1.

[10] Ohtake, Y., Belyaev, A. and Seidel, H-P. 3D scattered data interpolation and approximation with multilevel compactly supported RBFs. *Graphical Models* (2005) **67**:150–165.

[11] Wendland, H. *Scattered Data Approximation*. Cambridge University Press, (2005), ISBN: 0521843359.

[12] Prieto, J.L., An RBF-reconstructed, polymer stress tensor for stochastic, particle-based simulations of non-Newtonian, multiphase flows. *J. Non-Newtonian Fluid Mech.* (2016) **227**:90–99.

[13] Chenl, X. and Yang, V., Thickness-based adaptive mesh refinement methods for multi-phase flow simulations with thin regions. *J. Comput. Phys.* (2014) **269**:22–39.

[14] Yue, P., Feng, J.J., Liu, C. and Shen, J. Transient drop deformation upon startup of shear in viscoelastic fluids. *Phys. Fluids* (2005) **17**:123101.

[15] Aggarwal, N. and Sarkar, K. Effects of matrix viscoelasticity on viscous and viscoelastic drop deformation in a shear flow. *J. Fluid Mech.* (2008) **601**:63–84.

[16] Verhulst, K., Cardinaels, R., Moldenaers, P., Afkhami, S. and Renardy, Y. Influence of viscoelasticity on drop deformation and orientation in shear flow. Part 2: Dynamics. *J. Non-Newtonian Fluid Mech.* (2009) **156**(1-2):44–57.

[17] Prieto, J.L., Numerical simulations of buoyancy-driven droplets in non-Newtonian media using a variance-reduced, micro-macro, particle-level set

method. In: Kádár, R. (Ed.). *Annual Transactions of the Nordic Rheology Society* (2017) **25**:233–235.

[18] Prieto, J.L. and Carpio, J. Accurate and Efficient, Multiscale Simulations of Newtonian and non-Newtonian Free-Surface Flows. In: Papadrakakis, M. and Oñate, E. and Schrefler, B. (Eds.). *Proc. VII International Conference on Computational Methods for Coupled Problems in Science and Engineering* (2017) (7 pages).